Catalysis Science & Technology

PAPER

Cite this: *Catal. Sci. Technol.*, 2016, **6**, 1417

Microwave-assisted synthesis of porous Mn_2O_3 nanoballs as bifunctional electrocatalyst for oxygen reduction and evolution reaction†

Srabanti Ghosh,*[a] Prasenjit Kar,[a] Nimai Bhandary,[b] Suddhasatwa Basu,[b] Samim Sardar,[a] Thandavarayan Maiyalagan,[c] Dipanwita Majumdar,[d] Swapan Kumar Bhattacharya,[e] Asim Bhaumik,[f] Peter Lemmens[g] and Samir Kumar Pal[a]

Technological hurdles that still prevent the commercialization of fuel cell technologies necessitate designing low-cost, efficient and non-precious metals. These could serve as alternatives to high-cost Pt-based materials. Herein, a facile and effective microwave-assisted route has been developed to synthesize structurally uniform and electrochemically active pure and transition metal-doped manganese oxide nanoballs (Mn_2O_3 NBs) for fuel cell applications. The average diameter of pure and doped Mn_2O_3 NBs was found to be ~610 nm and ~650 nm, respectively, as estimated using transmission electron microscopy (TEM). The nanoparticles possess a good degree of crystallinity as evident from the lattice fringes in high-resolution transmission electron microscopy (HRTEM). The cubic crystal phase was ascertained using X-ray diffraction (XRD). The energy dispersive spectroscopic (EDS) elemental mapping confirms the formation of copper-doped Mn_2O_3 NBs. The experimental parameter using trioctylphosphine oxide (TOPO) as the chelating agent to control the nanostructure growth has been adequately addressed using scanning electron microscopy (SEM). The solid NBs were formed by the self-assembly of very small Mn_2O_3 nanoparticles as evident from the SEM image. Moreover, the concentration of TOPO was found to be the key factor whose subtle variation can effectively control the size of the as-prepared Mn_2O_3 NBs. The cyclic voltammetry and galvanostatic charge/discharge studies demonstrated enhanced electrochemical performance for copper-doped Mn_2O_3 NBs which is supported by a 5.2 times higher electrochemically active surface area (EASA) in comparison with pure Mn_2O_3 NBs. Electrochemical investigations indicate that both pure and copper-doped Mn_2O_3 NBs exhibit a bifunctional catalytic activity toward the four-electron electrochemical reduction as well the evolution of oxygen in alkaline media. Copper doping in Mn_2O_3 NBs revealed its pronounced impact on the electrocatalytic activity with a high current density for the electrochemical oxygen reduction and evolution reaction. The synthetic approach provides a general platform for fabricating well-defined porous metal oxide nanostructures with prospective applications as low-cost catalysts for alkaline fuel cells.

Received 4th August 2015,
Accepted 16th September 2015

DOI: 10.1039/c5cy01264c

www.rsc.org/catalysis

[a] *Department of Chemical, Biological and Macromolecular Sciences, S. N. Bose National Centre for Basic Sciences, Block JD, Sector III, Salt Lake, Kolkata 700 098, India. E-mail: ghosh.srabanti@gmail.com, srabanti.ghosh@bose.res.in*
[b] *Chemical Engineering Department, Indian Institute of Technology Delhi, Hauz Khas, New Delhi 110016, India*
[c] *School of Chemistry, University of East Anglia, Norwich NR4 7TJ, UK*
[d] *Department of Chemistry, Barasat Government College, Barasat, Kolkata 700 124, India*
[e] *Physical Chemistry Section, Department of Chemistry, Jadavpur University, Kolkata 700 032, India*
[f] *Department of Materials Science, Indian Association for the Cultivation of Science, 2A & 2B Raja S. C. Mullick Road, Jadavpur, Kolkata 700 032, India*
[g] *Institute for Condensed Matter Physics and Laboratory for Emerging Nanometrology LENA, TU Braunschweig, Mendelssohnstraße 3, 38106 Braunschweig, Germany*

† Electronic supplementary information (ESI) available. See DOI: 10.1039/c5cy01264c

Introduction

In recent years, significant efforts have been devoted to the fabrication of metal oxides having a large surface area, superior thermal stability and possible utilization in fundamental research as well as technological applications.[1–4] Among the transition metal oxides, manganese oxide nanostructures are attractive due to their involvement in active redox reactions which are consequently beneficial for a broad range of electrochemical applications from energy storage in lithium ion batteries and fuel cells to water splitting and chemical sensing.[5–11] A prerequisite for such applications of oxide nanostructures is novel synthetic routes leading to low-cost and large-scale production of materials at the nanoscale with well-defined morphologies. Up to now, various methodologies

have been employed to synthesize manganese oxide; however, most of these complicated synthetic procedures are associated with high-temperature synthesis, low yield and they are time-consuming.[11–13]

The development of sustainable synthetic processes using alternative energy inputs and greener reaction media has been recognized as an alternative approach for large-scale production of functional materials.[14–16] In this regard, the microwave-assisted hydrothermal (MAH) method offers a rapid and highly reproducible technique for the preparation of metal oxide nanomaterials with several advantages such as reduced energy consumption, shorter reaction time and higher product yield.[17–19] The microwave-assisted synthesis of metal oxide nanostructures with various morphologies such as Co_3O_4, MnO_2 and TiO_2, *etc.*, has been well documented in the literature.[17,20] Rapid synthesis of ZnO nanostructures using a microwave-assisted approach to accelerate nucleation and growth has been previously reported by our group.[21] Although microwave-assisted growth has been in vogue for preparation of various metal oxide nanostructures for the past decade, the reports regarding manganese oxides are scarce.[19,22,23] Here, we have reported the synthesis of porous Mn_2O_3 nanoballs (NBs) through a microwave-assisted route, which are useful for electrocatalytic applications.

The implementation of environmentally-friendly clean energy technologies is a vital issue and an alternative to traditional fossil fuel, as fuel cell devices endow efficient clean energy production and conversion.[24,25] A considerable number of nanomaterials with superior electrocatalytic activity are emerging as a new class of electrode materials to fulfill the increasing demands for high power conversion and durability.[15,16,26] Recently, there has been immense interest in the design and development of highly efficient oxygen reduction reaction (ORR) and oxygen evolution reaction (OER) catalysts which can resolve the crucial issues related to fuel cells and rechargeable metal–air batteries.[27] Pt-based metals or alloys are regarded as robust and efficient catalysts for oxidation reactions but their high cost and limited abundance necessitate the exploitation of new non-precious metal catalysts.[28] On the other hand, precious metal oxide nanomaterials such as iridium dioxide (IrO_2) and ruthenium dioxide (RuO_2) have demonstrated the best overall performance for catalyzing ORR and OER.[29,30] Despite this activity, the development of an active material *via* a naturally abundant and economically viable method has remained an unresolved issue in energy conversion applications. In fact, the oxygen reduction reaction is a challenging reaction due to slower ORR kinetics and the stability of the cathode catalyst material under cycling in acidic or alkaline conditions during operation. However, one critical issue to be addressed is the lack of effective electrocatalysts for the four-electron ($4e^-$) reduction of O_2 (ORR) at a relatively low overpotential.[31] Accordingly, non-precious transition metal oxides and in particular, manganese oxides (MnO_x) have been regarded as alternative ORR catalysts with reasonable catalytic activity, low cost, and structural stability for primary alkaline-based fuel cells.[32–36] In contrast to other manganese oxides (Mn_3O_4 or MnO_2), little attention has been paid to exploring the potential of the catalytic activity of Mn_2O_3 nanostructured materials.[33–35] Suib *et al.* reported a manganese oxide (MnO_2) catalyst having a dual nature (OER and ORR catalysis), a potential alternative for high-cost Pt and its alloys, iridium, and ruthenium oxide catalysts.[36] Recently, mixed metal oxides displaying excellent catalytic activities have been investigated as one of the most promising candidates for ORR in an alkaline medium.[37,38] Muhler *et al.* described the excellent electrocatalytic activities of cobalt–manganese-based spinels as synergistic bifunctional catalysts for OER and ORR.[39]

In the present study, we developed a simple and convenient microwave-assisted approach for the controlled synthesis of pure and metal-doped Mn_2O_3 balls at the nanoscale. The structure and chemical composition have been studied along with the growth process and the merits of the MAH method using trioctylphosphine oxide (TOPO) as the chelating agent for the formation of Mn_2O_3 nanoballs are highlighted. To the best of our knowledge, this is the first report on the synthesis of porous Mn_2O_3 nanostructures with controlled shape and composition by the MAH method. A systematic investigation has been conducted in order to control the average size of the Mn_2O_3 nanostructures by optimizing the concentration of the chelating agent (TOPO) and moreover, a mechanism of the formation of the nanoballs has also been proposed. The cyclic voltammetry measurements have been employed to investigate the electrocatalytic activity of these Mn_2O_3 nanostructures for both oxygen reduction and evolution reaction.

Materials and methods

Materials

Manganese acetate dihydrate, copper chloride dihydrate, *n*-trioctylphosphine oxide (TOPO, 99%), and Nafion were purchased from Sigma Aldrich. Potassium bromide, ethylene glycol (EG), sodium sulfate and absolute alcohol were obtained from Merck. All other chemicals employed were of analytical grade and used without further purification.

Synthesis of Mn_2O_3

In a typical synthesis of Mn_2O_3, 0.03 mol manganese acetate dihydrate and 0.12 mol *n*-trioctylphosphine oxide were dissolved in 30 ml of ethylene glycol. The resultant mixture was continuously stirred for 2 hours and then transferred into a 30 mL Teflon-lined stainless-steel autoclave. EG has been a selected as a polar and high microwave absorbing solvent. The Teflon-lined autoclave was microwave-heated to 120 °C and maintained at this temperature for 5 hours. The final product was collected and washed with distilled water and absolute alcohol at least three times. Then the as-prepared samples were further annealed at 450 °C for 6 hours in air. The effect of TOPO concentration on the formation of Mn_2O_3 was studied by preparing precursors with different molar ratios of Mn^{2+}:TOPO of 1:1, 1:2 and 1:4. The

synthesis of copper ion-doped manganese oxide nanoballs (designated as Cu–Mn_2O_3 NBs) was made by addition of 0.003 M copper chloride dihydrate under similar reaction conditions. In another set, 0.03 mol manganese acetate dehydrate and 1.2 mol urea were added into 30 ml of ethylene glycol to prepare Mn_2O_3 without using TOPO.

Characterization

Transmission electron microscopy (TEM) grids were prepared by applying a diluted drop of the Mn_2O_3 and Cu–Mn_2O_3 samples to carbon-coated copper grids. Field Emission Scanning Electron Microscopy (FESEM, QUANTA FEG 250) investigations were performed by applying a diluted drop of Mn_2O_3 and Cu–Mn_2O_3 nanoballs on silicon wafer. The phase structures of the as-prepared samples were determined by powder X-ray diffraction (XRD, PANalytical XPERTPRO diffractometer equipped with Cu Kα radiation at 40 mA and 40 kV, and a scanning rate of 0.02° S^{-1} in the 2θ range from 20° to 80°). The FTIR spectra of the as-prepared samples were recorded on a JASCO FTIR-6300 spectrometer, using KBr pellets. The thermal gravimetric analysis (TGA) of Mn_2O_3 solid powder was performed under nitrogen atmosphere with a heating rate of 10 °C min^{-1} from 30 °C to 1000 °C by using a Perkin-Elmer TGA-50H. A Quantachrome Autosorb 1-C was used to record the N_2 adsorption/desorption isotherm of the sample. The sample was degassed at 200 °C for 8 h under high vacuum conditions prior to the measurement.

Electrochemical measurements

For voltammetry measurements, a three-electrode cell was used with Ag/AgCl as the reference electrode and a Pt wire as the counter electrode. The electrolyte comprised of a 0.5 M aqueous Na_2SO_4 solution. The working electrode was fabricated by coating catalysts on a glassy carbon substrate. For electrode preparation, 2 mg of Mn_2O_3 and Cu–Mn_2O_3 were dissolved in 20 μl of ethanol containing 5 wt% Nafion as a binder. Then 10 μl of sample solution was deposited on the glassy carbon (working electrode). A multichannel potentiostat–galvanostat system (AutoLab 302 N) was used for cyclic voltammetry (CV) and for charge–discharge cycling studies in a potential window of −0.2 to 0.8 and at different scan rates of 5–50 mV s^{-1}.

To evaluate the electrochemical activity for the ORR of Mn_2O_3, rotating disk electrode (RDE) experiments were performed. Pt wire and Ag/AgCl (Sat. KCl) were used as the counter and reference electrodes, respectively, and 0.1 M KOH was used as an electrolyte. High-purity O_2 gas was purged for 30 mins before each RDE experiment to make the electrolyte saturated with O_2. A rotating disk electrode voltammetric study was carried out using a RRDE-3A Rotating Ring Disk Electrode Apparatus (BioLogic Science Instruments, France) connected to a DY2300 potentiostat (Digi-Ivy Inc., USA) at a scan rate of 10 mV s^{-1} and potential range from 0 to −0.6 V. A catalyst ink was prepared by ultrasonically mixing 6.0 mg of Mn_2O_3 sample with 3 mL of pure deionized water and 10 μL of 5 wt% Nafion solution for 1 h in order to make a homogeneous suspension. Then, 5 μL of prepared catalytic ink was transferred to the surface of a glassy carbon electrode of 3 mm diameter using a micropipette. Finally, the ink was allowed to dry for 10 min at room temperature to form a thin catalyst film on a glassy carbon electrode as a working electrode.

To evaluate the electrochemical activity for the oxygen evolution reaction (OER) of the Mn_2O_3, rotating disk electrode (RDE) experiments were performed under saturated N_2. Pt wire and Ag/AgCl (saturated KCl) were used as the counter and reference electrodes, respectively, and 0.1 M KOH was used as an electrolyte.[40] Electrochemical characterization was conducted using a single potentiostat with a scan rate of 10 mV s^{-1} and a potential range from 0 to 1 V. The ink was prepared according to the method described above for the ORR. Koutecky–Levich plots (J^{-1} *vs.* $\omega^{-1/2}$) were analyzed at various electrode potentials. The slopes of their best linear fit lines were used to calculate the number of electrons transferred (n) on the basis of the Koutecky–Levich equation:[41]

$$\frac{1}{j} = \frac{1}{j_L} + \frac{1}{j_K} = \frac{1}{B\omega^{\frac{1}{2}}} + \frac{1}{j_K} \tag{1}$$

$$B = 0.62\, nFC_0 \left(D_0\right)^{\frac{3}{2}} v^{-\frac{1}{6}} \tag{2}$$

$$j_K = nFkC_0 \tag{3}$$

where j (mA cm^{-2}) is the measured current density, j_K and j_L (mA cm^{-2}) are the kinetic and diffusion-limiting current densities, ω is the angular velocity of the rotating disk ($\omega = 2\pi N$, N is the linear rotating speed in rpm), n is the overall number of electrons transferred in ORR, F is the Faraday constant (96 485 °C mol^{-1}), C_0 is the bulk concentration of O_2 (1.2×10^{-6} mol cm^{-3}), D_0 is diffusion coefficient of O_2 (1.9×10^{-5} cm^2 s^{-1}), v is the kinematic viscosity of the electrolyte (0.01 cm^2 s^{-1}), and k is the electron transfer rate constant.[42] According to eqn (1) and (2), the number of electrons transferred (n) and the kinetic-limiting current j_K can be obtained from the slope and intercept of the Koutecky–Levich plots (J^{-1} *versus* $\omega^{-1/2}$).

Results and discussion

Synthesis and characterization of Mn_2O_3 nanostructures

The Mn_2O_3 and Cu-doped Mn_2O_3 were synthesized by a microwave-assisted hydrothermal method and the structural as well as the electrochemical properties of the as-prepared oxide samples were examined by common techniques as discussed below. The sizes and morphologies of the Mn_2O_3 samples were characterized by transmission electron microscopy (TEM) (Fig. 1).

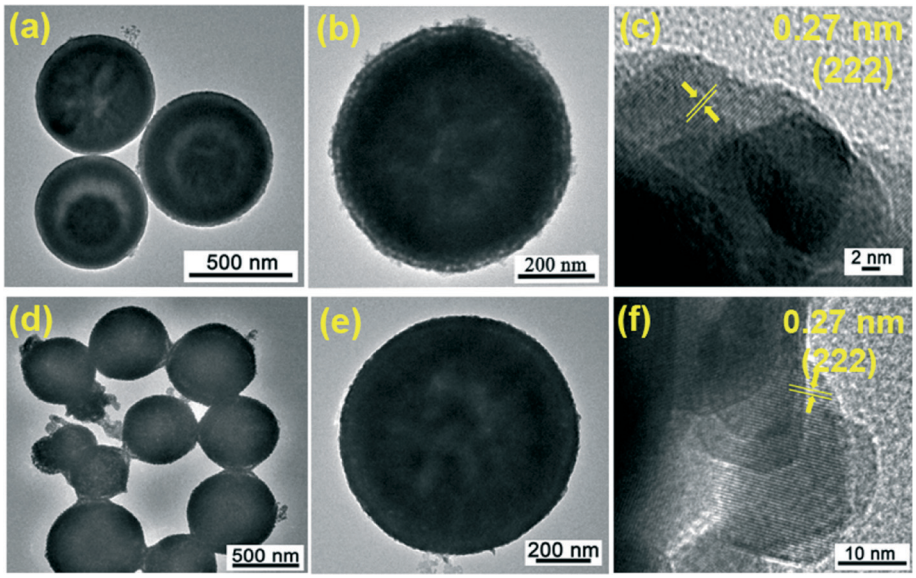

Fig. 1 Transmission electron microscopy (TEM) images of Mn_2O_3 and Cu-doped Mn_2O_3 nanoballs. (a) and (b) TEM images at different magnifications and (c) HRTEM image of Mn_2O_3 NBs. (d) and (e) TEM images at different magnifications and (f) HRTEM image of Cu–Mn_2O_3 NBs.

Fig. 1a illustrates the formation of the well-ordered spherical type Mn_2O_3 nanoballs (NBs) with a mean diameter of 550–620 nm. As evident from Fig. 1b, the NBs were fabricated by the aggregation of small particles, which presumably led to a rough surface. In addition, the intrinsic crystal structure of the as-prepared NBs was further characterized by high-resolution transmission electron microscopy (HRTEM). As shown in Fig. 1c, the interplanar distance between the fringes is found to be about 0.27 nm consistent with the (222) planes of Mn_2O_3.[13] The similar structure of Mn_2O_3 after Cu doping as revealed by the representative TEM images (Fig. 1d and e) suggests that doping might have not influenced the growth of the NBs. The Cu–Mn_2O_3 NBs exhibited a slightly bigger size ranging from 550–650 nm. The HRTEM image also demonstrated the highly crystalline nature of Cu–Mn_2O_3 NBs with a cubic phase (Fig. 1f). The shape of the NBs was found to be small grains of 5–10 nm diameter. Hence, highly crystalline and pure cubic phase Mn_2O_3 could be obtained under a mild temperature through the MAH synthesis.

The X-ray diffraction (XRD) patterns were recorded to confirm the lattice facets of Mn_2O_3 and Cu–Mn_2O_3. Fig. 2a shows the XRD patterns of pure and doped Mn_2O_3 and the diffraction peak position could be readily indexed as a cubic phase Mn_2O_3 crystal (JCPDS No. 41-1442). It is evident from the differences between the breadths of the XRD reflections that doping increases the crystallinity of the Mn_2O_3 structures. No other impurity peaks have been detected in both cases, indicating that the highly crystalline pure and metal-doped manganese oxides have been successfully synthesized using the microwave irradiation process. Moreover, FTIR analysis was carried out to investigate the chemical structure of trioctylphosphine oxide (TOPO) after microwave irradiation followed by the Mn_2O_3 NBs formation. Fig. 2b illustrates the FTIR spectra of pure TOPO and annealed Mn_2O_3 NBs. It appears that the band at 1145 cm^{-1} (P═O symmetric type) and 1468 cm^{-1} (CH_3 bending) of TOPO disappeared after microwave irradiation and followed by hydrothermal treatment, suggests the surface of NBs free from organic ligands which can be ideal for catalytic application.[43]

Thermogravimetric analysis of Mn_2O_3 powder showed a weight loss of ~8% up to 580 °C which should be attributed to the removal of surface-adsorbed water which is consistent with previous reports.[44] Moreover, the weight remains nearly unchanged which suggests a high thermal stability of the as-prepared Mn_2O_3 NBs (Fig. 2c). Similarly, Cu-doped Mn_2O_3 demonstrated a high thermal stability with ~5% weight loss up to 800 °C.

Further, the N_2 adsorption–desorption measurement was performed to determine the surface area analyses of Mn_2O_3 NBs. As shown in Fig. 2d, a type IV isotherm with an H3 hysteresis loop can be observed which confirms the mesoporosity of Mn_2O_3 NBs. Pore size distributions (PSD) of Mn_2O_3 NBs have been estimated by employing the non-local density functional theory (NLDFT) as shown in the inset of Fig. 2d, which suggests mesopore diameters centered at 1.8 nm and 3.7 nm. The Brunauer–Emmett–Teller (BET) surface area and pore volume are 22 $m^2\ g^{-1}$ and 0.038 $cm^3\ g^{-1}$, respectively, which are comparable with the manganese oxide nanostructures synthesized by other common methods.[45,46]

The FESEM images revealed that the Mn_2O_3 has a spherical morphology with a mean diameter of 600–860 nm (Fig. 3a). Moreover, at a higher magnification (Fig. 3b and c), it has been found that these solid NBs were formed by the self-assembly of very small nanoparticles as evident from the SEM image (Fig. 3b and c).

Mn_2O_3 demonstrated a homogeneous size distribution and the average diameter of the NBs prepared from 4 equivalents of TOPO (Mn^{2+} : TOPO, 1 : 4) was estimated to be ~600

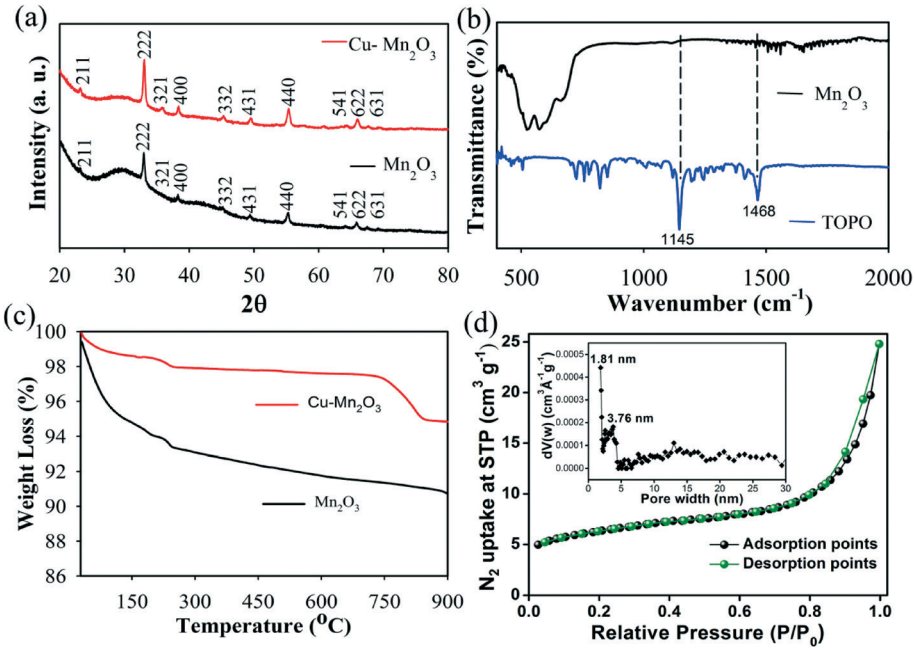

Fig. 2 Structural characterization of Mn_2O_3 and Cu-doped Mn_2O_3 nanoballs. (a) XRD patterns of Mn_2O_3 and Cu-doped Mn_2O_3 NBs. (b) FTIR spectra of trioctylphosphine oxide (TOPO) and Mn_2O_3 NBs. (c) Thermogravimetric analysis (TGA) profile of Mn_2O_3 and Cu–Mn_2O_3 NBs. (d) N_2 adsorption and desorption isotherms of porous Mn_2O_3 NBs. Adsorption and desorption points are marked by black and red symbols, respectively. Inset: the pore size distribution pattern employing the non-local density functional theory (NLDFT).

nm. The control over the morphology of Mn_2O_3 NBs using TOPO as the chelating agent which plays a dual role of controlling the chemical reaction from both the thermodynamic and kinetic aspects, has been confirmed further using urea as the structure-controlling agent (Fig. 3d–f). In the control experiment, the microwave-assisted hydrothermal decomposition of manganese salt without using TOPO did not produce any visible precipitate of manganese oxide. On the other hand, an equivalent amount of a very common capping as well as reducing agent, urea, has been used, but micrometric aggregates were obtained with an average size of ~2 to 10 μm under similar reaction conditions.[46] At a higher magnification, porous-cracked flake structures have been observed as shown in (Fig. 3f). This suggests that the formation and morphology of the as-prepared Mn_2O_3 NBs strongly depended on the presence of TOPO. It has to be noted that the chemical

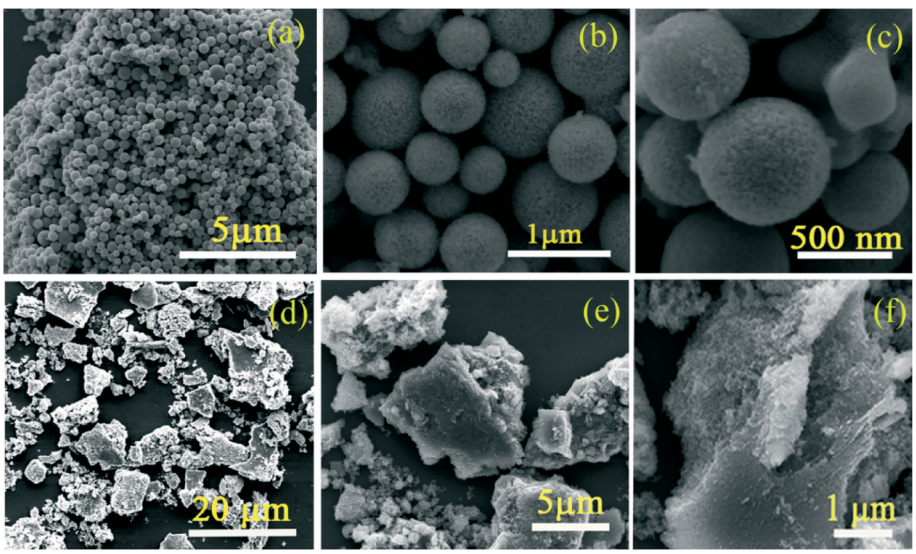

Fig. 3 Scanning electron microscopy (SEM) images of Mn_2O_3 nanoballs at different magnifications using TOPO and urea as structure-controlling agents. (a–c) SEM images of Mn_2O_3 NBs prepared using TOPO as the capping ligand (Mn^{2+} : TOPO, 1 : 4). (d–e) SEM images of Mn_2O_3 prepared using urea as the capping ligand (Mn^{2+} : urea, 1 : 4).

structure of TOPO has a tetrahedral structure with three long carbon chains, which differs significantly from the linear chain of the urea ligand.[47] The major chemical binding interaction of TOPO with the metal oxide surface is through the oxygen. Due to the unique structural feature of the TOPO molecule and lower intermolecular interaction, the density of the TOPO molecules at Mn_2O_3 NB surfaces is expected to be lower. Consequently, the particle growth in the presence of TOPO is well controlled *via* lower intermolecular interactions.[48] It has been further supported with density functional theory (DFT) calculation that due to the strong chemical interaction between the O atom of TOPO and the metal site, the formation of metal oxide clusters was stabilized.[49] On the other hand, a weaker N–M chemical bond primarily provides the main contribution toward the intermolecular interaction with the metal oxide surface along with the formation of N–H···O hydrogen bond in the case of urea. Hence, due to the strong chemical interaction between TOPO and the metal precursors, morphology-controlled Mn_2O_3 nanostructures have been achieved in the present case.

For a better understanding of the formation of these porous NBs, the concentration of TOPO, (metal: TOPO concentration ratio of 1.5 to 4) and the reaction time were varied during the synthesis. The average sizes of these Mn_2O_3 NBs can be tuned by controlling the concentration of TOPO. As discussed above, when the reaction was carried out at a ratio of 1 : 4, porous NBs were obtained (Fig. 3). The average diameter of Mn_2O_3 NBs produced was strongly dependent on the TOPO concentration and no dependency has been observed on the reaction time (data not shown). At a lower precursor concentration (1 : 1.5), micron-sized solid balls were obtained with a 1.2 μm average diameter, as shown in Fig. 4a–c. Further increasing the precursor concentration to 1 : 2, NBs typically ranging from 750 nm to 830 nm in diameter were obtained with an aggregated structure (Fig. 4d–f at a different magnification). The driving force by TOPO as a chelating agent dominates the Mn_2O_3 NBs formation and at a higher ratio, uniform nucleation and controlled growth facilitate the formation of uniform NBs. Hence, a higher concentration of TOPO might be preferable for the formation of uniform NBs, whereas relatively lower reactant concentrations could result in micron-sized slightly irregular balls in the MAH synthesis procedure.

Fig. 5a–c illustrated the morphology of the as-synthesized Cu^{+2}-doped Mn_2O_3 NBs as evident from FESEM. The average diameter of the Cu–Mn_2O_3 NBs was found to be 800 nm higher in comparison with pure Mn_2O_3 NBs, which is consistent with the TEM image. The elemental distribution of the material was further characterized by energy dispersive spectroscopic (EDS) mapping. The EDS elemental mapping clearly confirmed the presence and distribution of Mn, O, and Cu elements in the Cu–Mn_2O_3 NBs as shown in Fig. 5c–f. The EDS spectrum indicates that 8 wt% of Cu has been doped into the Mn_2O_3 crystal lattice (Fig. 5g).

On the basis of the experimental results, a possible formation mechanism of Mn_2O_3 NBs was proposed. Initially, Mn_2O_3 nuclei can form through the reaction between Mn^{2+} cations and O^- anions in the microwave-solvothermal process and further Mn_2O_3 nuclei grow to nanocrystals which are unstable under the solvothermal conditions. Consequently, they self-assemble into solid NBs and spontaneously adjust themselves to share the common crystallographic orientation driven by the minimization of the surface energy of the nanocrystals. This leads to the assembly of these nanocrystals, which is well documented in the literature.[50] Due to the high viscosity of ethylene glycol, the energy of the Brownian motion of the Mn_2O_3 nanocrystallites is not large enough to fully counterbalance the van der Waals interaction between the nanoparticles, forming spherical agglomerates of Mn_2O_3.[51]

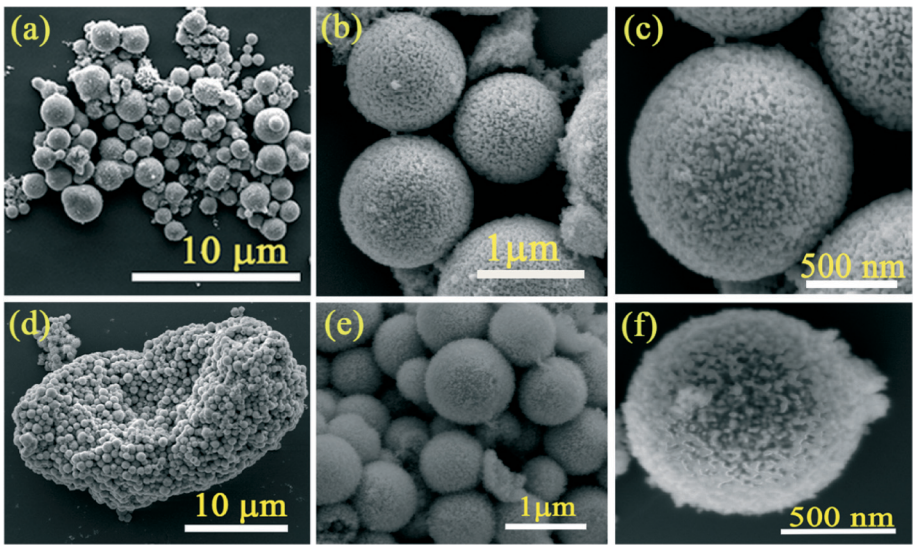

Fig. 4 Scanning electron microscopy (SEM) images of Mn_2O_3 nanoballs at different magnifications and varied concentrations of TOPO. (a–c) SEM images of Mn_2O_3 NBs prepared using Mn^{2+} : TOPO, (1 : 2) and (d–f) SEM images of Mn_2O_3 NBs prepared using Mn^{2+} : TOPO, (1 : 1).

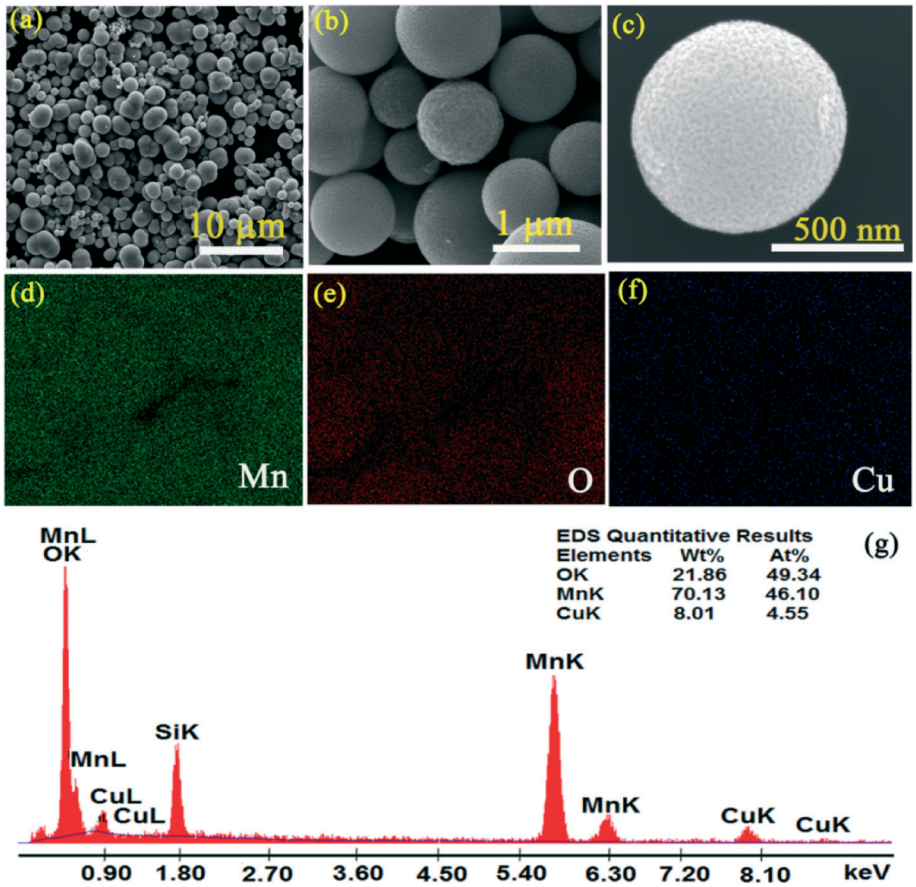

Fig. 5 SEM images and elemental mapping of Cu-doped Mn_2O_3 nanoballs. (a–c) SEM images at different magnifications, (d) Mn, (e) O, (f) Cu elemental mapping and (g) EDS spectrum of Cu-doped Mn_2O_3 NBs (using Mn^{2+} : TOPO, 1 : 4).

Electrochemical properties of Mn_2O_3 nanostructures

Before the electrocatalytic investigation, it is crucial to measure the electrochemically active surface area, an important factor associated with electrode reaction rates and double-layer parameters.[52] The electrochemically active surface areas (EASA) of the Mn_2O_3 and Cu–Mn_2O_3 electrodes have been estimated by considering the ratio of the electrochemical double-layer capacitance of the catalytic surface (C_{dl}) and the double layer capacitance of an atomically smooth planar surface of the material per unit area (C_s, specific capacitance) under the same electrolyte conditions.[53] Further, C_{dl} can be determined by measuring the non-Faradaic capacitive current related with double-layer charging from the scan rate dependence of the cyclic voltammograms (CVs). A typical CV of Mn_2O_3 and Cu–Mn_2O_3 NBs has been shown at a scan rate of 50 mV s^{-1} between −0.2 and 0.8 V (*vs.* Ag/AgCl) (Fig. 6a). The double-layer charging current (i_c) is equal to the product of the scan rate (v) and the double-layer capacitance (C_{dl}) as given by the following eqn.

$$i_c = vC_{d1} \quad (4)$$

Hence, a plot of i_c *versus* v follows a straight line with a slope equal to the C_{dl} as shown in Fig. 6(b). The current *vs.* scan rate in Fig. 6b does not pass through the origin and shows an intercept on the current axis at the zero scan rate which is not clear at this level. The estimated C_{dl} values of Mn_2O_3 and Cu–Mn_2O_3 were 0.018 mF and 0.097 mF. Specific capacitance values for carbon electrode materials have been reported in the range of C_s = 0.005–0.055 mF cm^{-2} in an alkaline medium.[54] We used a specific capacitance of C_s = 0.020 mF cm^{-2} for both Mn_2O_3 and Cu–Mn_2O_3 as representative reported values.

The estimated EASA values of Mn_2O_3 and Cu–Mn_2O_3 are 3.7 cm^2 and 19.46 cm^2. The EASA value of Cu–Mn_2O_3 is 15 times higher than that of Mn_2O_3. Galvanostatic discharge/charge measurements were performed in a potential range of −0.2 to 0.7 V (*vs.* Ag/AgCl). Upon galvanostatic charging/discharging, a slow discharge process was observed for Mn_2O_3 after 10 cycles as evidenced by a voltage drop (IR drop) and a bent discharge curve indicating that the stored energy could not be delivered in a fast manner (Fig. 6c and d). In contrast, the Cu–Mn_2O_3 can be charged/discharged rapidly even after 100 cycles, showing a well-defined discharge straight line. The high EASA value and the nearly triangular charge/discharge curves indicate that a nearly ideal electrical-double-layer capacitive behavior of the Cu–Mn_2O_3 can open up exciting opportunities for energy storage application.

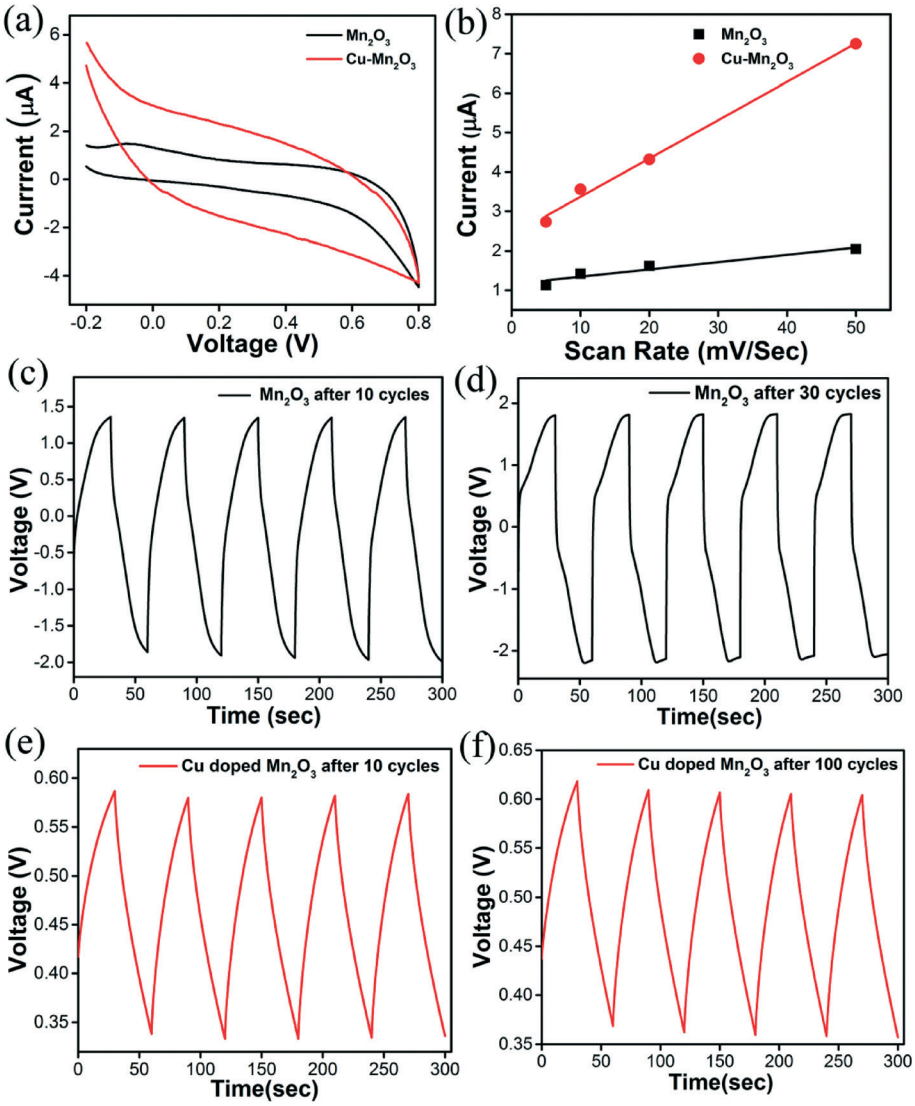

Fig. 6 Electrochemical properties of Mn_2O_3 and Cu-doped Mn_2O_3 nanoballs. (a) Representative cyclic voltammograms of Mn_2O_3 (black line) and Cu-doped Mn_2O_3 (red line) NBs in the potential range of −0.2 V to +0.8 V *versus* Ag/AgCl reference electrode (non-Faradaic region) at a scan rate of 50 mV s^{-1} in a N_2-saturated 0.5 M Na_2SO_4 solution. (b) The cathodic charging current measured as a function of scan rate (5 mV s^{-1}, 10 mV s^{-1}, 20 mV s^{-1}, and 50 mV s^{-1}) for Mn_2O_3 NBs and Cu–Mn_2O_3 NBs. (c) and (d) Galvanostatic charge–discharge curves of Mn_2O_3 NBs after 5 and 30 cycles. (e) and (f) Galvanostatic charge–discharge curves of Cu–Mn_2O_3 NBs after 5 and 100 cycles.

Electrocatalytic activity of Mn_2O_3 nanostructures

Manganese oxides are well known as efficient catalysts and the controlled synthesis of Mn_2O_3 nanomaterials prompts us to evaluate the catalytic properties.[55,56] The electrocatalytic performance of the Mn_2O_3 and Cu–Mn_2O_3 NBs for the oxygen reduction reaction (ORR) was characterized by CV in 0.1 M KOH on glassy carbon electrodes (with equal mass loading). The CV curves of the catalysts are shown at a scan rate of 50 mV s^{-1} in O_2-saturated and N_2-saturated 0.1 M KOH solutions (Fig. 7a and b). Compared with the nearly featureless reduction current in N_2-saturated electrolyte, the detected current under O_2 atmosphere was attributed to the catalytic oxygen reduction. RDE measurements were further carried out to reveal the ORR kinetics of the as-prepared catalysts.

As shown in Fig. 8(a), the ORR onset potential of the Mn_2O_3 electrode commenced at around −0.36 V. A clear reduction pre-wave was observed at a low overpotential which suggests efficient electrocatalytically active sites of Mn_2O_3 NBs for oxygen reduction. The RDE polarization curves at different rotation rates are used to study the kinetics of the Mn_2O_3 NBs. With the increase in rotation rate, mass transport at the electrode surface improves, leading to the enhancement of the current density (0.9 mA cm^{-2}) (Fig. 8b). From the analysis of the Koutecky–Levich plot, the value of n was found to be in the range of 3.16–3.8, which is close to the theoretical value for the $4e^-$ reduction of O_2 as shown in Fig. 8c. Oxygen can be directly reduced to water with the concomitant consumption of four electrons per O_2 molecule (eqn (5)). Alternatively, oxygen can be reduced indirectly,

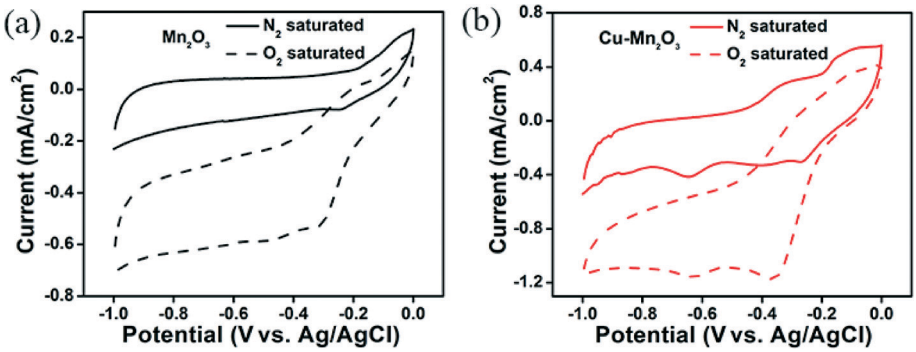

Fig. 7 Electrochemical properties of Mn_2O_3 and Cu-doped Mn_2O_3 nanoballs. Cyclic voltammetry curves for (a) Mn_2O_3 NBs and (b) Cu–Mn_2O_3 NBs on glassy carbon electrodes in O_2-saturated and N_2-saturated 0.1 M KOH solutions at a scan rate of 50 mV s^{-1}.

forming H_2O_2 as an intermediate and only two electrons per O_2 molecule are consumed (eqn (6)):

$$O_2 + 2H_2O + 4e^- \rightarrow H_2O + 4OH^- \quad (5)$$

$$O_2 + 2H_2O + 2e^- \rightarrow H_2O_2 + 2OH^- \quad (6)$$

This indicates that the Mn_2O_3 NBs possess a good electrocatalytic activity toward the $4e^-$ reduction of O_2 through a redoxmediated mechanism and sequential disproportionation of the reduction intermediates of O_2 reduction (*i.e.*, superoxide and peroxide ion in alkaline media).

To evaluate the OER activity, CV of the thin films of Mn_2O_3 NBs on glassy carbon electrodes was performed in N_2-saturated 0.1 M KOH solution. A set of polarization curves (Fig. 8d) were recorded on RDE at different rotating speeds to quantitatively verify the apparent 4 electron reaction on Mn_2O_3 NBs. The anodic current started at 0.6 V (*vs.* the reversible hydrogen electrode, RHE) with a maximum current density of 1 mA cm^{-2} at 1 V for Mn_2O_3 NBs. Similarly, the

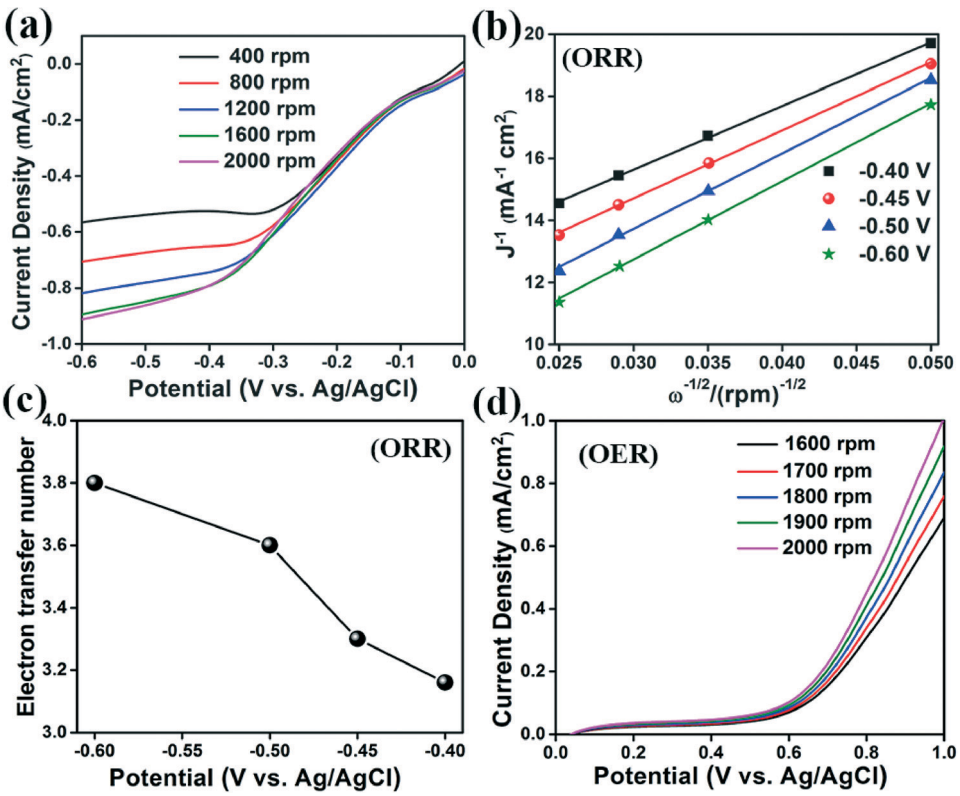

Fig. 8 Catalytic activity of Mn_2O_3 nanoballs for the oxygen reduction reaction (ORR) (a–c) and oxygen evolution reaction (OER) (d). (a) Rotating disk voltammograms in O_2-saturated 0.1 M KOH at different rotation rates for the oxygen reduction on the Mn_2O_3 NBs electrodes. (b) The corresponding Koutecky–Levich plots (J^{-1} *vs.* $\omega^{-0.5}$) at different potentials of Mn_2O_3 NBs. (c) The electron transfer number (n) profiles obtained from Koutecky–Levich plots. (d) Rotating disk voltammograms in N_2-saturated 0.1 M KOH at different rotation rates for the oxygen evolution on the Mn_2O_3 NBs electrodes.

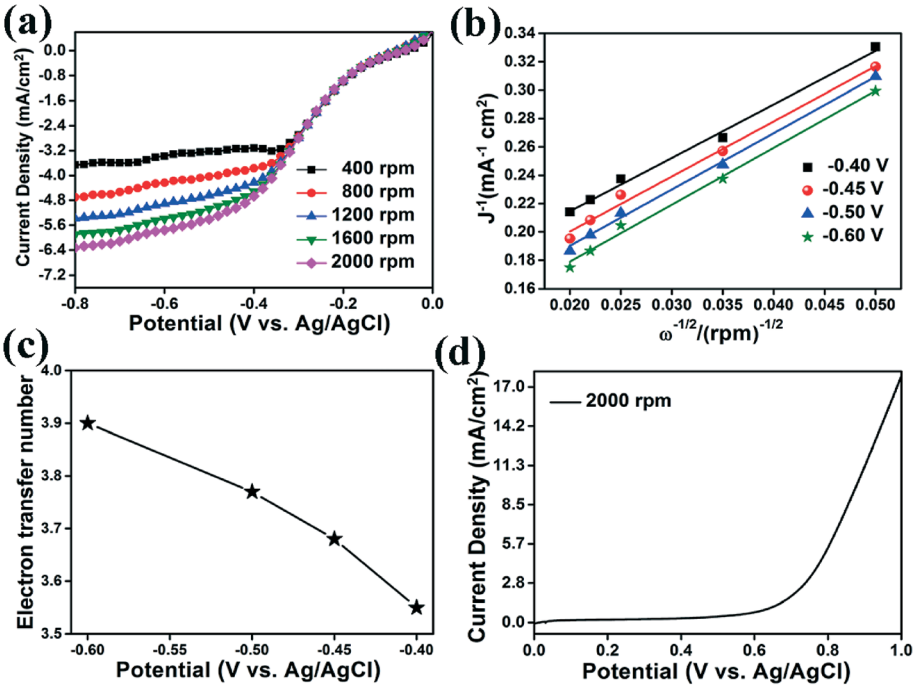

Fig. 9 Catalytic activity of copper-doped Mn_2O_3 nanoballs for the oxygen reduction reaction (ORR) and oxygen evolution reaction (OER). (a) Rotating disk voltammograms of Cu–Mn_2O_3 in O_2-saturated 0.1 M KOH at different rotation rates for the oxygen reduction. (b) The corresponding Koutecky–Levich plots (J^{-1} *vs.* $\omega^{-0.5}$) at different potentials of Cu–Mn_2O_3 NBs. (c) The electron transfer number (n) profiles obtained from Koutecky–Levich plots. (d) Representative rotating disk voltammogram in N_2-saturated 0.1 M KOH at 2000 rpm rotation rates for the oxygen evolution on the Cu–Mn_2O_3 NBs electrodes.

Cu-doped Mn_2O_3 NBs exhibited a bifunctional catalytic activity for both OER and ORR (Fig. 9a–c). ORR polarization curve of Cu–Mn_2O_3 NBs with the increase in rotation rate, leading to the enhancement of the current density ~5.8 mA cm^{-2} as shown in Fig. 9b. The Koutecky–Levich plot follows parallel straight lines for different potentials in mixed kinetic-diffusion-controlled regions, indicating the number of electrons transferred per O_2 molecule and the active surface area for the reaction do not change significantly within the potential range studied (Fig. 9b). From the analysis of the Koutecky–Levich plot, the value of n was found to be in the range of 3.4–3.9 (Fig. 9c). For OER, the anodic current with a maximum current density of 17 mA cm^{-2} at 1 V for Cu–Mn_2O_3 NBs has been achieved, which is much higher than that of the Mn_2O_3 NBs, as shown in Fig. 9d. This increase in current density might be due to the fact that the catalysts stimulate not only the oxygen evolution reaction but also the redox couple due to the presence of Cu in the Mn_2O_3 crystals as well as increasing the effective surface area ultimately improving catalytic efficiency which is consistent with earlier reports.[57,58] We further compared the catalytic activity of pure and Cu-doped Mn_2O_3 NB catalysts with other catalysts (Table S1†). Although the Pt/C, a state-of-the-art Pt catalyst, showed a higher activity, non-precious transition metal-based catalysts have shown excellent ORR activity in an alkaline medium.

The stability of the as synthesized catalysts was investigated by chronoamperometric (CA) measurements where the

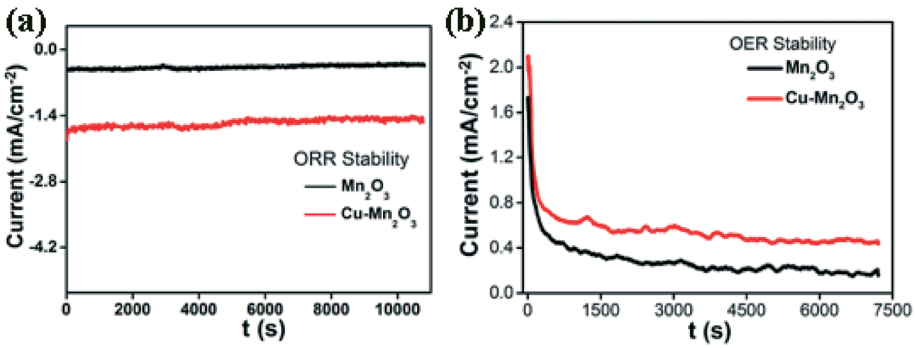

Fig. 10 Stability of pure and copper-doped Mn_2O_3 nanoballs for the oxygen reduction reaction (ORR) and oxygen evolution reaction (OER). Chronoamperometric curves for the (a) ORR and (b) OER of pure Mn_2O_3 NBs (black curve) and copper-doped Mn_2O_3 (red curve) NBs.

current density–time (*I vs. t*) curves at constant potentials were recorded as shown in Fig. 10. Both Mn_2O_3 NBs and Cu–Mn_2O_3 NBs exhibited distinct long-term choronoamperometic stability which is one of the key challenges for alkaline fuel cells. The ORR current values obtained for both Mn_2O_3 and Cu–Mn_2O_3 NBs were highly stable over 10 000 s of continuous operation at a constant potential of −0.4 V as shown in Fig. 10a.

During the chronoamperometric measurement for OER, initially, both catalysts exhibited a pronounced current decay, which could be caused by the accumulation of gas bubbles which may partially block the active sites of the electrode. The current density attained a steady state in the first ~700 s thereafter, indicating that both Mn_2O_3 NB catalysts form a very stable film on the glassy carbon electrode surface and also exhibit stable electrocatalytic performance towards OER. The excellent durability of the as-synthesized catalysts for both ORR and OER has been associated with the unique structural and chemical stability of the transition metal oxides in an alkaline medium.

Conclusion

In summary, we have successfully developed a facile and large-scale synthesis of thermally stable, crystalline, pure and copper-doped Mn_2O_3 NBs by a microwave-assisted hydrothermal method. More importantly, the low cost of the synthetic method combined with their promising bifunctional catalytic activity makes Mn_2O_3 NBs as a new class of electrocatalysts for the next generation fuel cells. Doped Mn_2O_3 NBs showed an improvement in the charge– discharge over the pure Mn_2O_3 NBs, which may be suitable for high-energy storage devices. The pure and doped Mn_2O_3 NBs can be effectively used as electrode materials with an electrocatalytic activity toward the 4-electron oxygen reduction reaction. Copper doping in Mn_2O_3 NBs reveals the enormous impact on the electrocatalytic activity with a high current density both for ORR and OER, which is supported with 5.2 times higher electrochemically active surface area (EASA) in comparison with pure Mn_2O_3. The pure and doped Mn_2O_3 NBs also exhibited stability for both ORR and OER under alkaline conditions, demonstrating that they can be used as effective electrocatalysts for alkaline fuel cells. Hence, the microwave-assisted approach is suitable for the synthesis of electrochemically active Mn_2O_3 nanostructures that are highly desirable for energy conversion and storage and can also be extended to prepare other transition metal-doped metal oxide for fuel cell applications.

Author contributions

S. G. planned the research, performed the experiment, analyzed the data and contributed to the writing of the manuscript. P. K. conducted the synthesis and characterization of the nanoballs. N. B. and S. B. performed the electrocatalytic activity experiments and helped in scientific discussion. S. S. helped in characterization and scientific discussion. T. M. helped in scientific discussion and manuscript writing. D. M. and S. K. B. carried out galvanostatic charge/discharge studies. A. B. performed N_2 adsorption–desorption measurements. P. L. helped in scientific discussion and manuscript writing. S. K. P. provided characterization measurements for catalysts. All authors reviewed the manuscript.

Acknowledgements

P. K. and N.B. thank the Council of Scientific and Industrial Research (CSIR, India) for fellowships. We thank the Department of Science and Technology (DST, India) for financial grants DST/TM/SERI/2 k11/103 and SB/S1/PC-011/2013. P. L. thanks the NTH-School "Contacts in Nanosystem: Interaction, Control and Quantum Dynamics", the Braunschweig International Graduate School of Metrology, DFG-RTG 1953/1, Metrology for Complex Nanosystems, and the German-Israel Foundation.

Notes and references

1 F. Wang, Z. Tan and Y. Li, Solution-Processable Metal Oxides/Chelates as Electrode Buffer Layers for Efficient and Stable Polymer Solar Cells, *Energy Environ. Sci.*, 2015, **8**, 1059–1091.

2 P. Kar, S. Sardar, S. Ghosh, M. R. Parida, B. Liu, O. F. Mohammed, P. Lemmens and S. K. Pal, Nano Surface Engineering of Mn2o3 for Potential Light-Harvesting Application, *J. Mater. Chem. C*, 2015, **3**, 8200–8211.

3 Z. Zhang, J. Liu, J. Gu, L. Su and L. Cheng, An Overview of Metal Oxide Materials as Electrocatalysts and Supports for Polymer Electrolyte Fuel Cells, *Energy Environ. Sci.*, 2014, **7**, 2535–2558.

4 S. Sardar, P. Kar, S. Sarkar, P. Lemmens and S. K. Pal, Interfacial Carrier Dynamics in Pbs-Zno Light Harvesting Assemblies and Their Potential Implication in Photovoltaic/Photocatalysis Application, *Sol. Energy Mater. Sol. Cells*, 2015, **134**, 400–406.

5 T. T. Truong, Y. Liu, Y. Ren, L. Trahey and Y. Sun, Morphological and Crystalline Evolution of Nanostructured Mno2 and Its Application in Lithium–Air Batteries, *ACS Nano*, 2012, **6**, 8067–8077.

6 G. Shen, P.-C. Chen, K. Ryu and C. Zhou, Devices and Chemical Sensing Applications of Metal Oxide Nanowires, *J. Mater. Chem.*, 2009, **19**, 828–839.

7 P. R. Solanki, A. Kaushik, V. V. Agrawal and B. D. Malhotra, Nanostructured Metal Oxide-Based Biosensors, *NPG Asia Mater.*, 2011, **3**, 17–24.

8 P. Zhang, Y. Zhan, B. Cai, C. Hao, J. Wang, C. Liu, Z. Meng, Z. Yin and Q. Chen, Shape-Controlled Synthesis of Mn3o4 Nanocrystals and Their Catalysis of the Degradation of Methylene Blue, *Nano Res.*, 2010, **3**, 235–243.

9 A. Giri, N. Goswami, M. Pal, M. T. Zar Myint, S. Al-Harthi, A. Singha, B. Ghosh, J. Dutta and S. K. Pal, Rational Surface Modification of Mn3o4 Nanoparticles to Induce Multiple

Photoluminescence and Room Temperature Ferromagnetism, *J. Mater. Chem. C*, 2013, **1**, 1885–1895.

10 A. Giri, A. Makhal, B. Ghosh, A. K. Raychaudhuri and S. K. Pal, Functionalization of Manganite Nanoparticles and Their Interaction with Biologically Relevant Small Ligands: Picosecond Time-Resolved Fret Studies, *Nanoscale*, 2010, **2**, 2704–2709.

11 P. Li, C. Nan, Z. Wei, J. Lu, Q. Peng and Y. Li, Mn3o4 Nanocrystals: Facile Synthesis, Controlled Assembly, and Application, *Chem. Mater.*, 2010, **22**, 4232–4236.

12 G. Salazar-Alvarez, J. Sort, S. Suriñach, M. D. Baró and J. Nogués, Synthesis and Size-Dependent Exchange Bias in Inverted Core–Shell Mno|Mn3o4 Nanoparticles, *J. Am. Chem. Soc.*, 2007, **129**, 9102–9108.

13 G. Yang, W. Yan, J. Wang and H. Yang, Fabrication and Formation Mechanism of Mn2o3 Hollow Nanofibers by Single-Spinneret Electrospinning, *CrystEngComm*, 2014, **16**, 6907–6913.

14 S. Ghosh, N. A. Kouame, L. Ramos, S. Remita, A. Dazzi, A. Deniset-Besseau, P. Beaunier, F. Goubard, P. H. Aubert and H. Remita, Conducting Polymer Nanostructures for Photocatalysis under Visible Light, *Nat. Mater.*, 2015, **14**, 505–511.

15 S. Ghosh, H. Remita, P. Kar, S. Choudhury, S. Sardar, P. Beaunier, P. S. Roy, S. K. Bhattacharya and S. K. Pal, Facile Synthesis of Pd Nanostructures in Hexagonal Mesophases as a Promising Electrocatalyst for Ethanol Oxidation, *J. Mater. Chem. A*, 2015, **3**, 9517–9527.

16 S. Ghosh, A.-L. Teillout, D. Floresyona, P. de Oliveira, A. Hagège and H. Remita, Conducting Polymer-Supported Palladium Nanoplates for Applications in Direct Alcohol Oxidation, *Int. J. Hydrogen Energy*, 2015, **40**, 4951–4959.

17 Y.-J. Zhu and F. Chen, Microwave-Assisted Preparation of Inorganic Nanostructures in Liquid Phase, *Chem. Rev.*, 2014, **114**, 6462–6555.

18 M. B. Gawande, S. N. Shelke, R. Zboril and R. S. Varma, Microwave-Assisted Chemistry: Synthetic Applications for Rapid Assembly of Nanomaterials and Organics, *Acc. Chem. Res.*, 2014, **47**, 1338–1348.

19 H. Huang, S. Sithambaram, C.-H. Chen, C. King'ondu Kithongo, L. Xu, A. Iyer, H. F. Garces and S. L. Suib, Microwave-Assisted Hydrothermal Synthesis of Cryptomelane-Type Octahedral Molecular Sieves (Oms-2) and Their Catalytic Studies, *Chem. Mater.*, 2010, **22**, 3664–3669.

20 K. Manseki, Y. Kondo, T. Ban, T. Sugiura and T. Yoshida, Size-Controlled Synthesis of Anisotropic Tio2 Single Nanocrystals Using Microwave Irradiation and Their Application for Dye-Sensitized Solar Cells, *Dalton Trans.*, 2013, **42**, 3295–3299.

21 S. Sardar, P. Kar and S. K. Pal, The Impact of Central Metal Ions in Porphyrin Functionalized ZnO/TiO_2 for Enhanced Solar Energy Conversion, *Journal of Materials NanoScience*, 2014, **1**(1), 12–30.

22 Y. Li, J. Wang, Y. Zhang, M. N. Banis, J. Liu, D. Geng, R. Li and X. Sun, Facile Controlled Synthesis and Growth Mechanisms of Flower-Like and Tubular Mno2 Nanostructures by Microwave-Assisted Hydrothermal Method, *J. Colloid Interface Sci.*, 2012, **369**, 123–128.

23 B. Ming, J. Li, F. Kang, G. Pang, Y. Zhang, L. Chen, J. Xu and X. Wang, Microwave–Hydrothermal Synthesis of Birnessite-Type MnO_2 Nanospheres as Supercapacitor Electrode Materials, *J. Power Sources*, 2012, **198**, 428–431.

24 S. Chu and A. Majumdar, Opportunities and Challenges for a Sustainable Energy Future, *Nature*, 2012, **488**, 294–303.

25 H. A. Gasteiger and N. M. Markovic, Just a Dream-or Future Reality?, *Science*, 2009, **324**, 48–49.

26 Y. Jiao, Y. Zheng, M. Jaroniec and S. Z. Qiao, Design of Electrocatalysts for Oxygen- and Hydrogen-Involving Energy Conversion Reactions, *Chem. Soc. Rev.*, 2015, **44**, 2060–2086.

27 J. Zhang, Z. Zhao, Z. Xia and L. Dai, A Metal-Free Bifunctional Electrocatalyst for Oxygen Reduction and Oxygen Evolution Reactions, *Nat. Nanotechnol.*, 2015, **10**, 444–452.

28 N. Jung, D. Y. Chung, J. Ryu, S. J. Yoo and Y.-E. Sung, Pt-Based Nanoarchitecture and Catalyst Design for Fuel Cell Applications, *Nano Today*, 2014, **9**, 433–456.

29 K. A. Stoerzinger, L. Qiao, M. D. Biegalski and Y. Shao-Horn, Orientation-Dependent Oxygen Evolution Activities of Rutile Iro2 and Ruo2, *J. Phys. Chem. Lett.*, 2014, **5**, 1636–1641.

30 E. A. Paoli, F. Masini, R. Frydendal, D. Deiana, C. Schlaup, M. Malizia, T. W. Hansen and S. Horch, Stephens IEL and Chorkendorff I, Oxygen Evolution on Well-Characterized Mass-Selected Ru and Ruo2 Nanoparticles, *Chem. Sci.*, 2015, **6**, 190–196.

31 Y. Li, W. Zhou, H. Wang, L. Xie, Y. Liang, F. Wei, J.-C. Idrobo, S. J. Pennycook and H. Dai, An Oxygen Reduction Electrocatalyst Based on Carbon Nanotube-Graphene Complexes, *Nat. Nanotechnol.*, 2012, **7**, 394–400.

32 X. Deng and H. Tüysüz, Cobalt-Oxide-Based Materials as Water Oxidation Catalyst: Recent Progress and Challenges, *ACS Catal.*, 2014, **4**, 3701–3714.

33 E. M. Benbow, S. P. Kelly, L. Zhao, J. W. Reutenauer and S. L. Suib, Oxygen Reduction Properties of Bifunctional A-Manganese Oxide Electrocatalysts in Aqueous and Organic Electrolytes, *J. Phys. Chem. C*, 2011, **115**, 22009–22017.

34 Y. Gorlin and T. F. Jaramillo, A Bifunctional Nonprecious Metal Catalyst for Oxygen Reduction and Water Oxidation, *J. Am. Chem. Soc.*, 2010, **132**, 13612–13614.

35 Y. Gorlin, B. Lassalle-Kaiser, J. D. Benck, S. Gul, S. M. Webb, V. K. Yachandra, J. Yano and T. F. Jaramillo, In Situ X-Ray Absorption Spectroscopy Investigation of a Bifunctional Manganese Oxide Catalyst with High Activity for Electrochemical Water Oxidation and Oxygen Reduction, *J. Am. Chem. Soc.*, 2013, **135**, 8525–8534.

36 Y. Meng, W. Song, H. Huang, Z. Ren, S.-Y. Chen and S. L. Suib, Structure–Property Relationship of Bifunctional Mno2 Nanostructures: Highly Efficient, Ultra-Stable Electrochemical Water Oxidation and Oxygen Reduction Reaction Catalysts Identified in Alkaline Media, *J. Am. Chem. Soc.*, 2014, **136**, 11452–11464.

37 T. Maiyalagan, K. A. Jarvis, S. Therese, P. J. Ferreira and A. Manthiram, Spinel-Type Lithium Cobalt Oxide as a

Bifunctional Electrocatalyst for the Oxygen Evolution and Oxygen Reduction Reactions, *Nat. Commun.*, 2014, **5**, 3949–3956.

38 P. W. Menezes, A. Indra, N. R. Sahraie, A. Bergmann, P. Strasser and M. Driess, Cobalt–Manganese-Based Spinels as Multifunctional Materials That Unify Catalytic Water Oxidation and Oxygen Reduction Reactions, *ChemSusChem*, 2015, **8**, 164–171.

39 A. Zhao, J. Masa, W. Xia, A. Maljusch, M.-G. Willinger, G. Clavel, K. Xie, R. Schlögl, W. Schuhmann and M. Muhler, Spinel Mn–Co Oxide in N-Doped Carbon Nanotubes as a Bifunctional Electrocatalyst Synthesized by Oxidative Cutting, *J. Am. Chem. Soc.*, 2014, **136**, 7551–7554.

40 M. R. V. Lanza and R. Bertazzoli, Selection of a Commercial Anode Oxide Coating for Electro-Oxidation of Cyanide, *J. Braz. Chem. Soc.*, 2002, **13**, 345–351.

41 F. H. B. Lima, M. L. Calegaro and E. A. Ticianelli, Electrocatalytic Activity of Manganese Oxides Prepared by Thermal Decomposition for Oxygen Reduction, *Electrochim. Acta*, 2007, **52**, 3732–3738.

42 J. Qiao, L. Xu, L. Ding, P. Shi, L. Zhang, R. Baker and J. Zhang, Effect of Koh Concentration on the Oxygen Reduction Kinetics Catalyzed by Heat-Treated Co-Pyridine/C Electrocatalysts, *Int. J. Electrochem. Sci.*, 2013, **8**, 1189–1208.

43 M. Green, N. Allsop, G. Wakefield, P. J. Dobson and J. L. Hutchison, Trialkylphosphine Oxide/Amine Stabilised Silver Nanocrystals-the Importance of Steric Factors and Lewis Basicity in Capping Agents, *J. Mater. Chem.*, 2002, **12**, 2671–2674.

44 G. D. Mukherjee, S. N. Vaidya and C. Karunakaran, High Pressure and High Temperature Studies on Manganese Oxides, *Phase Transitions*, 2002, **75**, 557–566.

45 Z. Cai, *et al.* Manganese Oxide/Carbon Yolk–Shell Nanorod Anodes for High Capacity Lithium Batteries, *Nano Lett.*, 2015, **15**, 738–744.

46 Q. Li, L. Yin, Z. Li, X. Wang, Y. Qi and J. Ma, Copper Doped Hollow Structured Manganese Oxide Mesocrystals with Controlled Phase Structure and Morphology as Anode Materials for Lithium Ion Battery with Improved Electrochemical Performance, *ACS Appl. Mater. Interfaces*, 2013, **5**, 10975–10984.

47 V. V. T. Doan-Nguyen, P. J. Carroll and C. B. Murray, Structure Determination and Modeling of Monoclinic Trioctylphosphine Oxide, *Acta Crystallogr., Sect. C: Struct. Chem.*, 2015, **71**, 239–241.

48 P. W. Sadik, S. J. Pearton, D. P. Norton, E. Lambers and F. Ren, Functionalizing Zn- and O-Terminated Zno with Thiols, *J. Appl. Phys.*, 2007, **101**, 104514–104518.

49 J. Chang and E. R. Waclawik, Experimental and Theoretical Investigation of Ligand Effects on the Synthesis of Zno Nanoparticles, *J. Nanopart. Res.*, 2012, **14**, 1012–1025.

50 K.-S. Cho, D. V. Talapin, W. Gaschler and C. B. Murray, Designing Pbse Nanowires and Nanorings through Oriented Attachment of Nanoparticles, *J. Am. Chem. Soc.*, 2005, **127**, 7140–7147.

51 C. Tian, W. Li, Q. Zhang, K. Pan and H. Fu, Controllable Fabrication of Various ZnO Micro/Nanostructures from a Wire-Like Zn–Eg–Ac Precursor *Via* a Facile Solution-Based Route, *Mater. Res. Bull.*, 2011, **46**, 1283–1289.

52 S. Trasatti and O. A. Petrii, Real Surface Area Measurements in Electrochemistry, *Pure Appl. Chem.*, 1991, **63**, 711–734.

53 C. C. L. McCrory, S. Jung, J. C. Peters and T. F. Jaramillo, Benchmarking Heterogeneous Electrocatalysts for the Oxygen Evolution Reaction, *J. Am. Chem. Soc.*, 2013, **135**, 16977–16987.

54 S. K. Bikkarolla, P. Cumpson, P. Joseph and P. Papakonstantinou, Oxygen Reduction Reaction by Electrochemically Reduced Graphene Oxide, *Faraday Discuss.*, 2014, **173**, 415–428.

55 A. Yamaguchi, R. Inuzuka, T. Takashima, T. Hayashi, K. Hashimoto and R. Nakamura, Regulating Proton-Coupled Electron Transfer for Efficient Water Splitting by Manganese Oxides at Neutral Ph, *Nat. Commun.*, 2014, **5**, 4256–4261.

56 F. Cheng, J. Shen, B. Peng, Y. Pan, Z. Tao and J. Chen, Rapid Room-Temperature Synthesis of Nanocrystalline Spinels as Oxygen Reduction and Evolution Electrocatalysts, *Nat. Chem.*, 2011, **3**, 79–84.

57 D. Strmcnik, D. F. van der Vliet, K. C. Chang, V. Komanicky, K. Kodama, H. You, V. R. Stamenkovic and N. M. Marković, Effects of Li^+, K^+, and Ba^{2+} Cations on the Orr at Model and High Surface Area Pt and Au Surfaces in Alkaline Solutions, *J. Phys. Chem. Lett.*, 2011, **2**, 2733–2736.

58 C. H. Choi, H.-K. Lim, M. W. Chung, J. C. Park, H. Shin, H. Kim and S. I. Woo, Long-Range Electron Transfer over Graphene-Based Catalyst for High-Performing Oxygen Reduction Reactions: Importance of Size, N-Doping, and Metallic Impurities, *J. Am. Chem. Soc.*, 2014, **136**, 9070–9077.